ChemEngineering

Article

Energy Recovery from Iron Ore Sinter Using an Iron Oxide Packed Bed

Sam Reis [1,*], Peter J. Holliman [1], Stuart Cairns [1], Sajad Kiani [1] and Ciaran Martin [2]

[1] Faculty of Science and Engineering, Swansea University, Singleton Park, Swansea SA2 8PP, UK
[2] Tata Steel UK Ltd., Port Talbot SA13 2NG, UK
* Correspondence: 902162@swansea.ac.uk

Abstract

This study investigated a novel method of recovering energy from iron ore sinter using solid iron oxide heat transfer materials. Traditionally, air is passed through the sinter either in an open conveyor or a sealed vessel to recover energy. The bed materials used were a magnetite concentrate, hematite ore, goethite–hematite ore and sinter fines. A shortwave thermal camera and quartz reactor were used measure infrared radiation from the process. The thermal imaging was combined with image analysis techniques to visualise the transfer of thermal energy through the system. The results showed that energy moved rapidly through the system with peak heating rates of 18 °C/min at a lump sinter temperature of 600 °C. The ratio of heating rate to cooling rate was as high as 8.6:1.0, indicating efficient retention of energy by the bed materials. The bed composition, determined by X-ray fluorescence and X-ray diffraction was used to calculate the heat capacity based on pure material properties. The resultant energy balance determined thermal efficiency to be between 32 and 46% for the sinter fines and hematite–goethite ore, resulting in predicted fuel savings of up to 9.4kg/tonne with similar heat utilisations to the air recovery process. Thermal imaging combined with Brunauer–Emmett–Teller surface area measurements and scanning electron microscopy analysis experimentally replicated mathematical heat transfer model predictions that a smaller total pore volume resulted in less thermally resistive bed. Image analysis illustrated the breaking of the heat front between the less resistive solid and more resistive air in porous beds versus even conduction of heat through a dense bed. The oxide distribution in the bed materials impacted heat transfer, as at a lump temperature of 500 °C was controlled by hydrated oxide content whereas at 600 °C Fe_2O_3 was the more dominant driver.

Keywords: energy recovery; iron ore sinter; thermography

Academic Editor: José P. Coelho

Received: 2 September 2025
Revised: 14 October 2025
Accepted: 17 October 2025
Published: 24 October 2025

Citation: Reis, S.; Holliman, P.J.; Cairns, S.; Kiani, S.; Martin, C. Energy Recovery from Iron Ore Sinter Using an Iron Oxide Packed Bed. *ChemEngineering* **2025**, *9*, 118. https://doi.org/10.3390/chemengineering9060118

1. Introduction

The production of iron ore sinter is an example of linear economy because it consumes large quantities of non-renewable fossil fuel that is combusted and emitted from the process as gaseous CO_2, thus increasing the concentration of greenhouse gas in the atmosphere [1]. The fuel rate of the process is dependent on the energy demand of the bed and the calorific value of the fuel, but typically loadings of 40–80 kg/tonne [2,3] are used, equating to 1471.80 MJ/tonne [4]. These energy demands must be considered in the context of wider sustainability goals because the steel industry is a key driver of a green future, with solar panels, wind turbines and sustainable buildings being steel intensive

technologies [5]. Therefore, in alignment with the United Nations (UN)sustainable development goals [6] and environmental targets set at the Conference of the Parties 2021 (COP21) [7], there has been substantial research into reducing fossil fuel consumption through energy recycling [8,9], biomass fuels [10,11], gaseous fuels [12,13] and improving fuel efficiency [3,14].

Sinter production is widely used to manufacture ferrous-based raw material for blast furnace ironmaking [15]. Temperatures of over 1300 °C are required to melt the raw mixture and initiate the melt solid reactions needed to begin to form the crucial silicoferrites of calcium and aluminium (SFCA) bonding phases [16]. Nicol et al. [17] produced a detailed review of the complex composition, crystal structure and morphology of SFCA. The overarching theme of this report was that the physical properties of the sinter were improved through cooling within a specific range of rates to facilitate optimal crystallisation. In line with this, Hsieh and Whiteman [18] used a laboratory furnace to control the heating and cooling of raw sinter and found that allowing the sinter to cool slowly (~3 °C/min) from a peak temperature of 1255 °C increased the proportion of stronger and more reducible SFCA-I crystalline phase content. They demonstrated that this increased the sinter's strength due to the reaction of magnetite and silicate melt. These data therefore suggest that sinter needs to transfer its stored thermal energy to allow its physical properties to develop sufficiently to survive the blast furnace. While the stored thermal energy of the sinter cannot be directly retained, it can be absorbed using an energy carrier and used in a different stage of the process. Sinter has been observed to exit the process at temperatures between 500 and 600 °C [19–21], which if efficiently captured could be used from ignition and preheating [22] to steam generation [23].

Heat recovery materials need to have a high heat capacity, be easy to handle and transport and be economically viable; thus, water and air are two very common heat transfer materials used in industry. Specifically tailored heat transfer fluids can also be used for applications outside of the operational range of water and air. Water is a particularly powerful heat transfer fluid due to its high heat capacity from hydrogen bonding [24], although its use with solid materials is restricted to quenching, as the energy is difficult to recover [25]. Because of iron ore sinters' large particle size and resistance to flow [26], packed beds are mainly used in industry. To recover energy from the sinter, it is passed onto a moving conveyor, where air is driven up through the bed by powerful fans. The air absorbs the thermal energy from the sinter via forced convection. Studies have simulated the process using 1-D [27], 2-D [28] and 3-D [29] models as well as utilising exergy [9] to optimise the process. Liu et al. [28] simulated the sintering process using a 2-D unsteady model, where individual slices in the 2-D time temperature model represent traveling down the bed. The calculations were carried out under the assumption of energy grades and cascade utilisation, whereby high temperature air >300 °C is used as combustion gas and any other air is used for preheating. The useful energy emitted from the cooling section of the sinter strand was in the range of 115–175 GJ/h, dependent on several different factors such as air flow rate and bed height. The dry quenching process uses an inert gas to cool and recover energy from incandescent coke breeze within a sealed reaction vessel [30]. The use of sinter in a "vertical tank" was numerically investigated by Dong et al. [31] as a solution to the air leakage problem in moving grate cooling systems [32]. Further research by Feng et al. [33–36] experimentally and numerically investigated the heat transfer coefficients, Ergun's correlation and the exergy characteristics of the vertical bed. Parameter optimisation by Feng et al. [37] found that 41.27 MW could be recovered using a sinter flow of 152 kg/s and an air flow of 180 kg/s in an 8 m high bed. Industrial applications of the vertical sinter cooler have experienced operational difficulties relating to airflow resistance and poor quality heat output [38].

Solid–solid heat transfer between high temperature slag has been used to generate bio-oil and char from the pyrolysis of biomass. As the main heat transfer mechanism was conduction, a higher slag surface area resulted in a greater heat transfer and oil production, while a lower surface area increased char production. Use of slags for gasification of solid wastes and biomass has been investigated by various other researchers [39]. While the direct use of energy from other granulated materials is relatively well documented, energy from iron ore sinter has traditionally been extracted using air [8]. Lower-temperature materials such as sinter are not applicable to biomass pyrolysis, but lower-temperature solid–solid processes may be the solution. Felinks et al. [39] hypothesised a solid–solid heat transfer process that utilised particles in separate size ranges to improve surface contact and separability. In their study, 0.8mm cerium oxide at 1000–1400 °C was contacted with 4 mm alumina spheres in a multistage process, recovering 70% of the thermal energy. The method in this paper diverges away from the use of air and exploits the thermal properties and size difference between sinter and iron ore to optimise heat transfer and improve the interaction with infrared radiation

Both the grate and vertical tank methods use air, 78% of which is nitrogen that interacts poorly with infrared radiation [40]. Infrared radiation strongly interacts with polar bonds, with bond frequencies of 2.5–20 μm causing stretching and vibration of the bonds. The quantity and type of polar bonds within a molecular structure determines their radiative properties. Hematite absorbs infrared light in two bands, 21.1–21.6 μm and 17.3–18.5 μm, which stretches the Fe-O bonds. The additional λO-H and δO-H bonds in goethite absorb at a higher frequency, 12.5 μm and 11.0–11.1 μm, than the hematite, therefore inferring more efficient energy absorption through the pores in the bed. Magnetite absorbs in between hematite and magnetite at 14.3–17.5 μm [41]. After absorption, the bonds relax back into a higher-energy state, increasing the bulk temperature of the material with excess energy re-emitted as infrared radiation where the ratio of incident to emitted radiation is known as the emissivity. The radiation that is not absorbed by the infrared (IR) active bonds can either be reflected or pass through a material, further affecting the quantity of photons incident to the camera and therefore the calculated temperature.

The authors' previous work [42] demonstrated the ability of lump sinter to efficiently absorb and transfer thermal energy because of their high emissivity and therefore interaction with infrared radiation. The emissivity of the lump sinter was found to range from 0.64–0.82 in the temperature range of 200–600°C in the 1–5μm range. Using these results, a hypothesis was developed that iron oxide materials could be effective in recovering thermal energy from iron ore sinter in a direct heat transfer process like that described by [40]. The increased density of solids compared to air will lead to a greater heat transfer per unit mass, and that direct transfer of energy between the hot lump sinter and bed materials will minimise transfer losses. The thermal energy absorbed by the material would be recycled back into the sintering process to reduce the fossil fuel rate. This study was designed based on measurements at the Taranto Ilva steel plant by Pelagagge, Caputo and Cardarelli [19,20] that showed that the sinter arrived at the cooling strand at a temperature between 500 and 600 °C at a rate of 9300 tonne/h. They found that an air flow rate of 27,000 tonne/h through the bed feeding to a preheating line recovered an average of 50 MW, with an air outlet temperature of 380 °C.

The experiments were performed at a laboratory scale incorporating infrared thermography to track and optimise heat flows in a novel energy capture methodology. The experiment aims to evaluate four different bed materials to determine the optimal bed chemistry and particle size for efficient heat recovery. The transition from using air to iron ore as a heat transfer material would be a radical shift for the steel industry and would provide an alternate option for heat recovery utilising current raw materials and minimal

new equipment. To the best of our knowledge, this study is the first to target a solid–solid heat transfer process to iron ore sintering and will provide a fundamental understanding of the dynamics of the process.

2. Bed Materials

Iron ore sintering is a well-developed and highly flexible process that, unlike other ironmaking processes which rely heavily on high-purity ore, can handle a wide range of iron oxide ores whilst maximising sinter product quality and minimising cost. Therefore, a representative set of raw materials were selected as bed materials here, including a magnetite concentrate, hematite-containing ore, hematite–goethite ore and sinter fines.

2.1. Particle Morphology

Previous studies have shown that heat transfer rate in packed beds is controlled by the ratio of conduction, convection and radiation in the bed [43]. Several physical and thermodynamic properties affect this ratio, but one of the most significant factors is particle morphology. To determine the particle morphology of the bed materials studied here (Table 1), high-resolution images were captured from directly above the powders using a 50-megapixel camera and processed in ImageJ (version 2) (Figure 1). Before imaging, the samples were laid out on a white background, ensuring, as much as possible, that individual particles were not touching each other. In ImageJ, the images were converted to 32bit greyscale and thresholded to the greyscale value of the background to create a mask. From this mask, the major and minor diameters (D_1 and D_2, respectively) of the particles were measured along with their perimeter (P) through automated pixel counts. Equation (1) was then used to calculate particle area (A), and subsequently, the circularity θ was calculated using Equation (2).

$$A = \pi\left(\frac{D_1}{2} * \frac{D_2}{2}\right) \quad (1)$$

$$\theta = \frac{4\pi A}{P^2} \quad (2)$$

Table 1. Key bed properties of the heat transfer mediums.

Bed Material	θ	D_{av}	M	M_t	ρ	ρ_t	ρ_b	α
-	-	mm	g	g	(kg m^{-3})	(kg m^{-3})	(kg m^{-3})	-
Sinter fines	0.77	2.65	59.09	63.31	791.92	848.49	3600	0.78
Magnetite concentrate	0.48	0.16	74.56	85.32	999.35	1143.45	5175	0.81
Hematite	1.01	0.22	69.82	81.27	935.70	1089.23	3670	0.75
Hematite–goethite	0.97	0.27	71.43	80.63	957.34	1080.69	5130	0.81

To calculate the density of each bed in a random packing scenario, ρ, the quartz reactor used in the subsequent experiments, V = 7.5 × 10^{-5} m^3, was completely filled and carefully levelled off using a ruler while avoiding compressing the mixture before being weighed. To measure preferential packing, ρ_t, the outside of the quartz reactor was tapped evenly around its circumference until the level of the sample stabilised reactor was then filled completely, levelled off and weighed again. The difference in the density established the maximum variance for the bed of material during the experiments. Using $\rho = \rho_f$ and the pure oxide density from [44–46] as ρ_b, the voidage of each medium was also calculated using Equation (3), where α = voidage, ρ_f = free density, ρ_{fl} = fluid density and ρ_b = bulk density.

$$\alpha = 1 - \frac{\rho_f - \rho_{fl}}{\rho_b - \rho_{fl}} \quad (3)$$

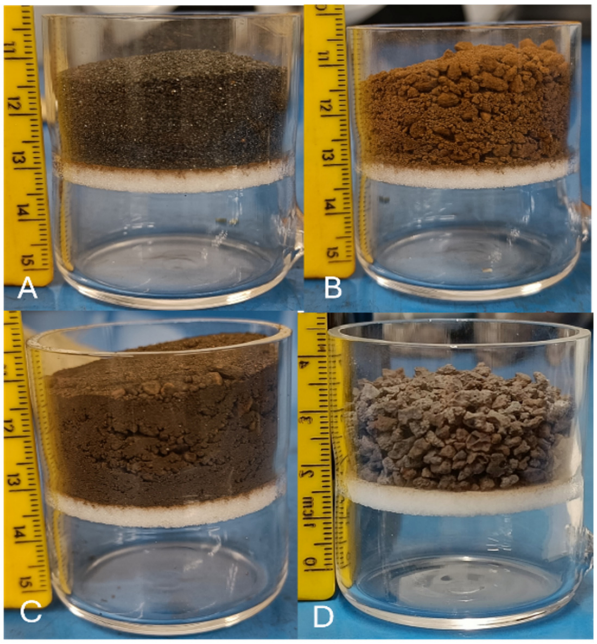

Figure 1. Pictures showing the distribution of particles for each bed in the quartz reactor. (**A**) = the magnetite concentrate, (**B**) = the hematite ore, (**C**) = the hematite–goethite ore and (**D**) = Sinter fines.

Detailed images of the bed materials were taken on an Quanta 600 field emission gun scanning electron microscope (SEM) (FEI company, Hillsboro, OR, USA), with the bed materials mounted on sticky carbon dots (Figure 2). The mounting method allowed the bed materials to be randomly sampled from the source material used for the heat recovery tests.

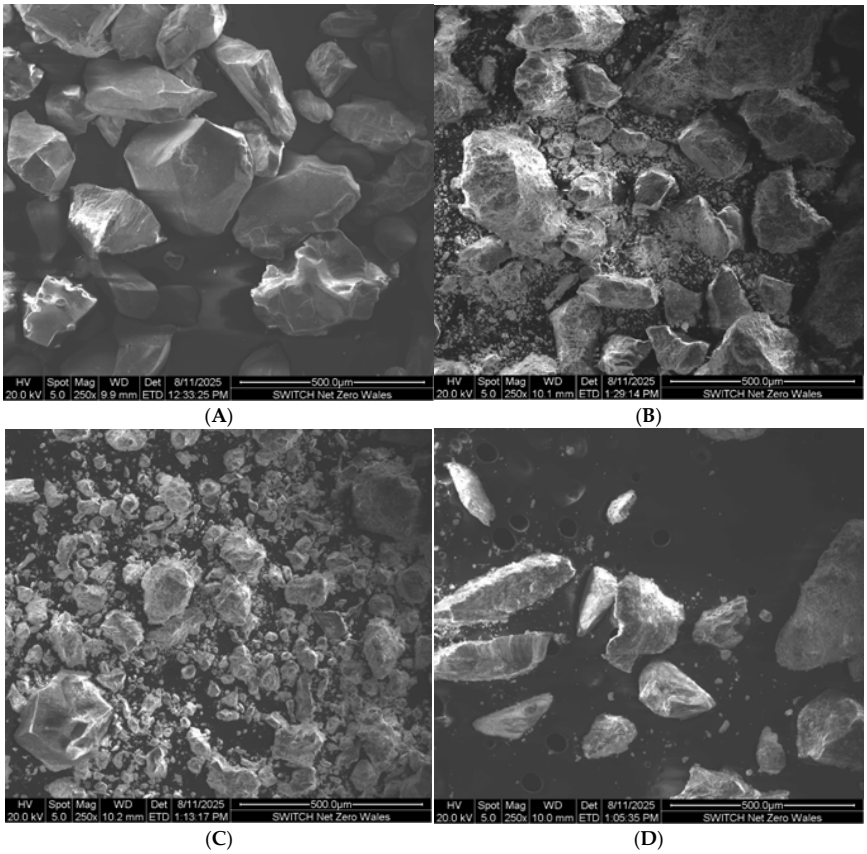

Figure 2. Backscattered SEM images of the bed materials at a 250× magnification, where (**A**) = magnetite concentrate, (**B**) = hematite ore, (**C**) = hematite–goethite ore and (**D**) = sinter fines.

The magnetite concentrate had smooth, angular particles with very few pores. The particles ranged from 52 μm to 352 μm. The angular nature of the particles would allow them to pack together effectively, producing high densities. Conversely, the hematite ore had more amorphous particles with a textured surface, increasing surface area. The particles were more amorphous than the magnetite particles but still had sharp angles. The hematite particles had a wider size range, with the largest particles having diameters of 323 μm and the smallest <10 μm. The hematite–goethite ore formed more spherical particles than the other bed materials, although their surface was rough, like the hematite ore. The particles ranged from 199 μm to <10 μm, marginally smaller than the hematite ore. The sinter fines formed long, angular particles that ranged from >400 μm to <10 μm. Their surface was textured in a similar way to the hematite ore. The large angular particles would contribute to low packing densities.

The higher-magnification images (Figure 3) show the surface texture and shape of each bed material in more detail. Additionally, they highlight the small (<10 μm) particles present in the hematite, hematite–goethite and sinter fines.

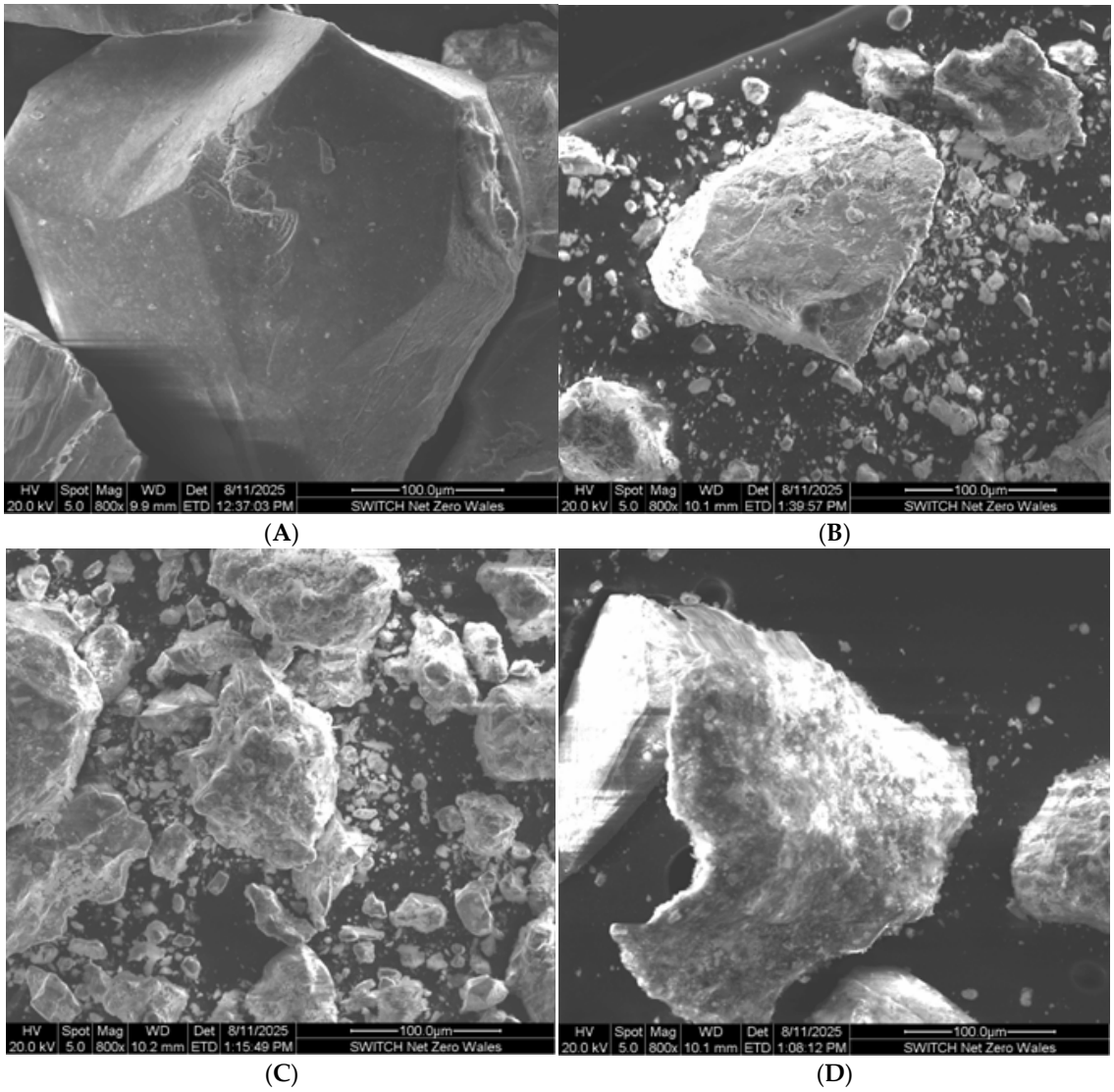

Figure 3. Backscattered SEM images of the bed materials at an 800× magnification, where (**A**) = magnetite concentrate, (**B**) = hematite ore, (**C**) = hematite–goethite ore and (**D**) = sinter fines.

2.2. Brunauer-Emmett-Teller (BET) Surface Area and Pore Structure

To characterise the heat transfer, nitrogen adsorption–desorption isotherms were conducted at 77 K using a Micromeritics Accelerated Surface Area and Porosity (ASAP) 2020 system (Eindhoven, Noord-Brabant, Netherlands). Specific surface area was measured using the Brunauer-Emmett-Teller (BET) method, while total pore volume and average pore diameter were obtained via the Barrett-Joyner-Halenda (BJH) method. These values give insight into pore accessibility and structural openness, complementing the bulk voidage and particle size data. Table 2 summarises the BET results for all bed materials.

Table 2. Textural characterisation of the heat transfer media (BET results).

Bed Material	BET Surface Area	Total Pore Volume	Average Pore Diameter
-	m^2/g	cm^3/g	nm
Hematite ore	11.1	0.0287	51.8
Magnetite concentrate	2.5	0.0074	58.0
Hematite–goethite ore	5.0	0.0146	58.5
Sinter fines	3.1	0.0084	54.0

3. Energy Balance

The accurate measurement of the chemical composition of the bed materials was performed using X-ray diffraction and fluorescence (XRD and XRF). To determine the hydrated content of the ores, non-isothermal thermogravimetric analysis (TGA) at a heating rate of 5 °C/min to 900 °C was conducted. The combination of these results (Table 3) was used to calculate the heat capacity of the lump sinter and the bed materials, which was then used to accurately evaluate the flow of energy through the system. The XRD results revealed the complex crystalline phases formed by the flux elements present, such as SFCA and calcium ferrite as well as the oxide state of the iron (Tables S1 and S2). Using this data, the pure material heat capacities from the literature were used to calculate a composite heat capacity for the lump sinter and bed materials [47–50]. The increased crystallographic detail of the XRD worked in tandem with the chemical analysis of the XRF to improve the accuracy of the model. To quantify the infrared absorption potential of the bed materials, their infrared absorption spectra was measured using an attenuated total reflectance Fourier transform infrared spectroscopy (FTIR) with a scan range of 4000–550 cm^{-1} at a 1 cm^{-1} resolution.

Table 3. Summary of the XRF, TGA and XRD results used to calculate the heat capacity of the bed materials.

-	XRF (%)		TGA (%)	XRD (%)		
Bed Material	Fe_T	Gangue	Mass Loss	Hematite	Magnetite	Goethite
Hematite ore	62.41	9.74	2.53	67.92	20.13	11.95
Magnetite concentrate	65.58	5.65	0.38	5.00	95.00	0.00
Hematite–goethite	58.02	12.54	2.32	64.00	0.00	21.00
Sinter fines	55.56	20.13	0.00	49.00	51.00	0.00

The thermal conductivity (T_c) of a material is defined by Equation (4), which multiplies the heat flux (Q) per unit area (A) by the temperature difference ΔT across a thickness (d).

$$T_c = \frac{Qd}{A\Delta T} \quad (4)$$

To calculate T_c, 20 g of each bed material was formed into a square with a thickness of 5 mm and placed on a hotplate set at 250 °C. A K-type thermocouple with a modified

flat tip was placed at 1 mm under the top surface of the bed material, and the lid of the hotplate was closed, Figure S1. The lid had a high-emissivity coating which reflected any radiated heat from the bed material back to the surface, reducing heat loss from the system. The hotplate supplied a constant heat flux of 13 W to the samples.

Moving on to the thermal conductivity data, Table 4 shows that the hematite–goethite ore had the highest thermal conductivity, closely followed by the magnetite concentrate. The thermal conductivity followed the trend of densities, as the sinter fines had the lowest conductivity and a much lower density than the ores. These values represent the conductivity of the bed materials at their free density ρ as they were in the experiments.

Table 4. Calculation parameters and results of the thermal conductivity tests of the bed materials.

-	T_f	t	A	h	K
Bed Material	**°C**	**s**	**m^2**	**m**	**W m^{-1} K^{-1}**
Magnetite concentrate	228	554	7.4×10^{-4}	5.3×10^{-3}	4.38
Hematite ore	211	345	8.9×10^{-4}	5.4×10^{-3}	2.07
Hematite–goethite ore	234	675	6.9×10^{-4}	5.0×10^{-3}	5.98
Sinter fines	170	208	9.0×10^{-4}	8.5×10^{-3}	1.55

4. Thermal Cycling

Iron oxides have been used as reactive elements for the production and transport of hydrogen through a cyclic reduction and oxidation reaction [51–53]. The iron oxides are first reduced to pure metals by a stream of CO, CH_4, H_2, etc., at high temperatures (>800 °C). The metallised product is then exposed to steam which re-oxidises the sponge iron, forming a pure hydrogen product [52]. The "steam-iron" process has been used commercially since the early 20th century. To improve the process, researchers have investigated the mechanical stability of the iron oxides over repeated thermal and chemical cycles [54]. Lorente et al. [51,52] found that an increase in non-iron oxides (Al, Ca and Si) increased the stability over multiple cycles compared to pure iron oxide, with Al_2O_3 having the most prominent effect. Otsuka et al. [55] used Brunauer–Emmett–Teller surface area measurements and scanning electron microscopy to measure the resistance to sintering of various additives. The BET data showed that after three redox cycles, the Al_2O_3 doped sample retained 56% of the original surface area compared to only 10% for pure iron oxide. Compositional analysis of the bed materials in this study showed that hematite–goethite ore had the highest Al_2O_3 concentration (1.73%), followed by the sinter fines and the hematite ore; however, the magnetite concentrate only had 0.03% Al_2O_3. These data show that within the single cycle system of heat transfer proposed by this study, magnetite would be the most susceptible to mechanical degradation in a scaled process. Because of this, the blend of the raw sinter mixture would need to be modified to retain the optimal particle size distribution within the raw sinter bed. In an iron ore sinter bed, an optimal ratio of particle sizes was a nuclei (1–3.3 mm) to adhering ($\leq$0.25 mm) ratio of 1.4 to create optimal bonds via liquid bridges creating quasi particles 6 [56,57].

5. Thermal Camera Calibration

The emissivity of the sinter was measured by heating sinter in a lab furnace for 2.5 h to ensure homogeneity between the thermocouple in the furnace and the actual sinter temperature. Images of the sinter were taken by the A6750 (Teledyne FLIR, Wilsonville, OR, USA) in the 1–5 μm region, as the door of the furnace was opened to reduce heat loss. Emissivity was adjusted in FLIR Research Studio until the sinter temperature matched the furnace temperature. An increase in emissivity is caused by electrons being pushed

into higher energy levels through the absorption of energy followed by re-emission of a proportion of that energy.

The emissivity of each bed material was measured by heating a 40 g sample of each in an oven to 100 °C for 2.5 h, as the maximum bed temperatures in the heat recovery experiments were found to be in the region of 100 °C. The sample was then taken out and placed directly underneath the A6750 camera and a K-type thermocouple inserted into the bed material. The temperature of the thermocouple was compared to the A6750 to calculate the emissivity at each temperature point as the bed material cooled. A new sample of the same bed material was then heated in the same way and placed in the quartz vessel along with the K-type thermocouple while being filmed by the A6750 placed perpendicular. Using the known value for the lump sinter's emissivity, the properties of the quartz reactor were calibrated. Two lumps of sinter were placed in the furnace for 2.5 h to reach equilibrium before being simultaneously removed and placed both in, and next to, the quartz reactor.

FLIR Research Studio was used to extract the temperature data from the A6750 by selecting the whole area of the sample in a rectangular area. From these areas, the average temperature of the sample was extracted and compared to the thermocouple data, and linear interpolation was then used to calculate the value of emissivity/transmittance for each temperature point. The emissivity and transmittance settings used on the A6750 for the heat transfer experiments are given in Table 5.

Table 5. Thermal parameters of the bed materials at a temperature of 100 °C used for each experiment based on calibration data.

Bed Material	Emissivity	Transmittance
Magnetite concentrate	0.95	0.4
Hematite ore	0.95	0.4
Hematite–goethite ore	0.95	0.45
Sinter fines	0.8	0.5

The results of the camera calibration tests (Table 5) determined that sinter fines had the lowest emissivity of the bed materials. The magnetite concentrate, the hematite ore and the hematite–goethite ore had the same emissivity value at this low temperature, but the hematite–goethite ore had a slightly different transmittance value. This indicated a slight shift in the wavelength of infrared emitted and therefore a differing absorption by the quartz. Before heating the magnetite, the concentrate was a dark grey colour, with the hematite and hematite–goethite ore having a more orange colouring. Lastly, the sinter fines were a light grey colour. It was observed that as the materials were heated in the furnace, their visual appearance darkened. The darkening of the bed materials potentially shows an increase in emissivity, although the colour of an object indicates how a material interacts with visible light rather than infrared. In the authors' previous study, the emissivity of lump sinter, predominantly iron oxide, increases with temperature, Table 6, in agreement with the literature data [58]. It is therefore likely that the emissivity of the bed materials increases when their temperature increases above 100 °C, but for the purpose of these experiments, the emissivity was fixed at the value for 100 °C.

Table 6. Temperature dependence of lump sinter emissivity measured using a shortwave (1–5 µm) A6750 thermal camera.

Temperature °C	Emissivity
200	0.64
250	0.66
300	0.7
350	0.71
400	0.73
450	0.74
500	0.79
600	0.82

The emissivity of the lump sinter was found to increase with temperature, with a range of 0.64–0.82 from 200–600 °C. There is a difference between the emissivity of the sinter fines and the lump sinter because of their chemistry with sinter fines having a lower level of the silico-ferrite of calcium and aluminium bonding phase than the lump sinter as well as a differing slag chemistry. Compared to the authors' previous work [42], the emissivity of the lump sinter is lower than the longwave region (7–14 µm).

6. Packed Bed Experiments

The experimental setup consisted of a quartz reaction vessel, a FLIR A6750 thermal camera, K-type thermocouple, thermocouple controller, laptop and laboratory furnace. The quartz vessel was transparent to infrared photons (Table 5), allowing the A650 to capture the photons emitted from the surface of the bed materials perpendicular to the reaction vessel at a distance of 1 m. The lump sinter was sampled from the 10–16 mm fraction from sinter pot tests using a hybrid biomass fuel, which is described in more detail in the authors' previous publication [42]. A bottom layer of 20 ± 0.01 g of bed material was added to the reaction vessel while the lump sinter samples were heated in a laboratory furnace to 500, 550 or 600 °C. After 2.5 h, a sinter sample was taken out of the furnace and placed in the vessel, a second 20 ± 0.01 g layer was added and the K-type thermocouple was inserted into the bed. The temperature of the bed throughout the experiment was monitored by the A6750 thermal camera. The K-type thermocouple was used to verify the accuracy of the thermal camera data.

The temperature profile of the first (bottom) and second (top) 20 g layer of bed material was measured individually using the region of interest feature on FLIR Research Studio (Figure 4). An example of the resultant temperature profile can be seen in Figure S2. The size of the regions of interest shown as the red dotted areas in Figure 4 were maximised to increase the measured area. In some experiments, the packing of the beds was such that the pore aligned, allowing photons from the surface of the lump sinter to reach the sensor of the A6750 camera, denoted as "gaps" in Figure 4. If these areas were included in the region of interest, the calculated temperature would be erroneous; therefore, the size of the region of interest was reduced to avoid these areas. The area of the regions of interest (ROIs) was varied for each bed material based on the packing arrangements (Table 1), as pores within the bed occasionally allowed photons from the lump sinter to reach the camera. In these cases, the ROIs were adjusted to maximise the measured area, avoiding the pores. The data gathered for analysis for each layer were the starting temperature and time (T_s, t_s); maximum temperature and time (T_m, t_m); and final temperature (60 °C) and time (T_f, t_f). These data points were exported into Excel (Microsoft, Redmond, WA, USA);

the rate of heating (*HR*) and cooling (*CR*) and the ratio between them were calculated using Equations (5)–(7).

$$HR = \frac{T_m - T_s}{t_m - t_s} \quad (5)$$

$$CR = \frac{T_m - T_f}{t_f - t_m} \quad (6)$$

$$R = \frac{HR}{CR} \quad (7)$$

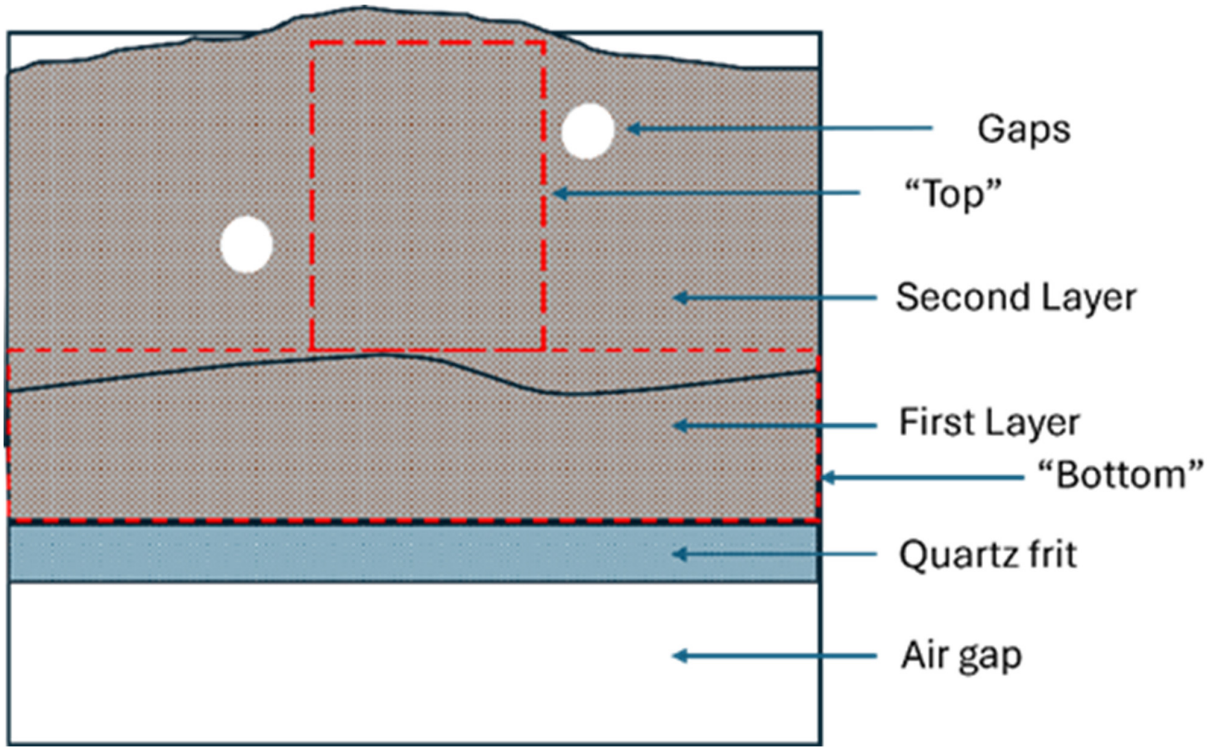

Figure 4. Diagram explaining the layout of the packed bed experiments and the placement of area selections in FLIR Research Studio.

Image Analysis

The flow of energy through the bed materials was investigated using the emission of photons from the surface of the bed materials measured by the A6750 thermal camera. In FLIR Research Studio, the colour palette of the thermal images was set to have a cut off at 60 °C, where the colour changed from white to orange. Subsequently, screenshots were taken every 10 s (300 frames), up to 120 s, as this showed the fastest section of heating. The image analysis program, ImageJ, was then used to threshold the images using the white–orange cutoff. The process of thresholding the images allowed quantitative evaluation of the total thresholded area and the number of isolated thresholded areas (hotspots).

7. Results and Discussion

7.1. Calibration Results

The particle size data (Table 1) clearly indicated that sinter fines had the largest average particle size (D_{av}) and subsequently the lowest bed density. The ores had a much smaller D_{av}, with the magnetite concentrate and the hematite ore having average diameters of 0.16 mm and 0.22 mm, respectively. Image analysis also showed the uniformity of the particles, with the magnetite concentrate having the most uniform particle size and the hematite ore the least, with a range in particle sizes from 0.067 mm to 8.63 mm. The variation in the size of the lump sinter (Table 1) was due to the pseudo random process

determined by the distribution of the bonding phase in the sintering process [59]. From XRD analysis (Tables S1 and S2), the phases present in the sinter and bed materials ranged from simple oxides such as hematite to more complex multi-element phases like SFCA. The heat capacity results for the lump sinter samples had a 3.5% deviation across the five samples, with an average value of 863.6, 892.1 and 919.9 J/kg K at 500, 550 and 600 °C, respectively (Figure 5). Lai et al. [50] calculated the heat capacity of sinter to be 860–980 J/kg K in the temperature range of 200–380 °C, whereas [28] used a value of 920 J/kg·K and a sinter inlet temperature of 550 °C in their simulation, which is very similar to the 600 °C but deviates quite significantly from the 500 °C (Figure 5).

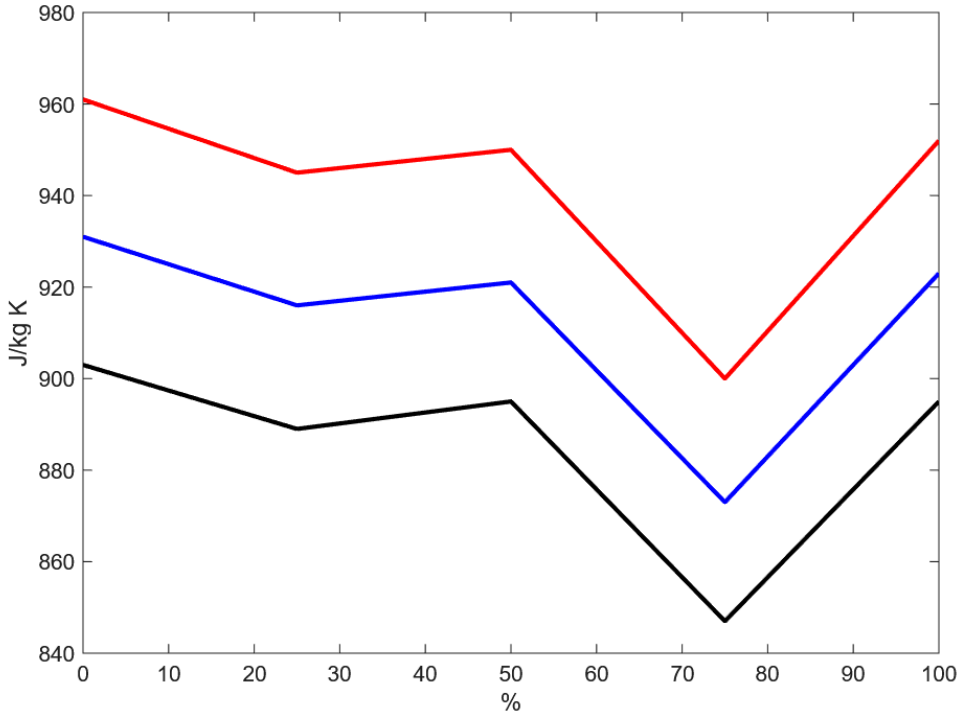

Figure 5. Heat capacity (J/kg K) of the lump sinter made using increasing ecoke content, where black = 500 °C, blue = 550 °C and red = 600 °C; dotted + squares = top layer and dashed + circles = bottom layer.

Comparing the heat capacity of the bed materials (Figure 6) at a standard temperature of 100 °C, the hematite–goethite ore was found to have the highest heat capacity, followed by the hematite ore, the sinter fines and the magnetite concentrate. The oxidation state of iron along with the bound water content had the largest impact on the heat capacity because of their increased interaction with infrared radiation compared to the gangue elements. Magnetite has a higher heat capacity than hematite, but the hydrogen bonding between the hydroxyl groups (FeOOH) in goethite increased its heat capacity (Table 3).

The polar bonds contained within the bed materials vibrated, stretched and twisted when they absorbed infrared radiation (Figure 7). Collected FTIR spectra showed peaks representing goethite, hematite, silicon and calcium oxides. The specific peak information is shown in Table S3. Hydrated iron oxides contain a mixture of the polar O-H and Fe-O bonds [60–62], resulting in a strong absorption, as shown in Figure 7, whereas magnetite only contains Fe-O, reducing the absorption potential. As expected, the hematite–goethite ore had a higher absorption peak compared to the magnetite concentrate. The breaking of O-H and Ca-O bonds in the high-temperature sintering process reduces the absorption potential, but the formation of silico ferrites of calcium and aluminium has been shown to have a positive effect [42], restoring the infrared absorption capability of sinter.

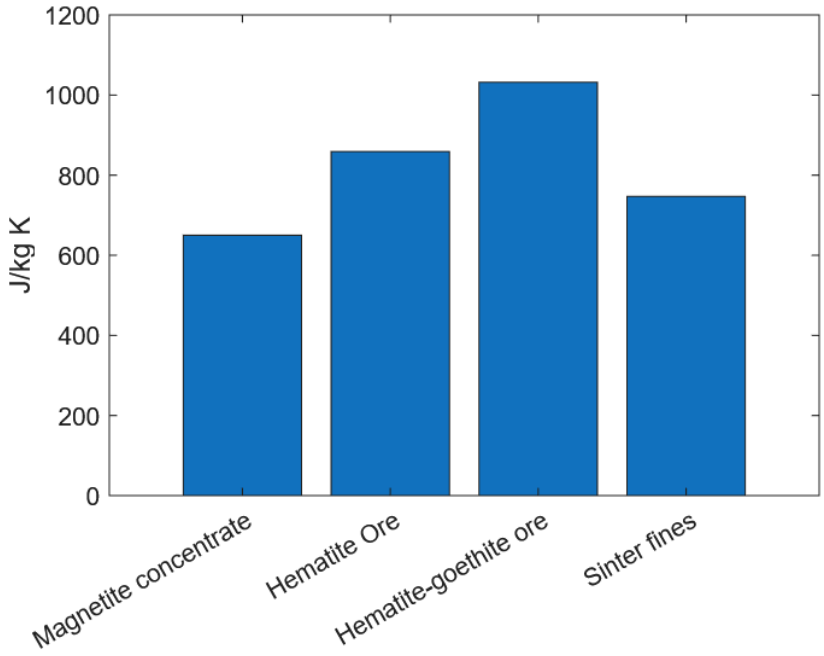

Figure 6. Heat capacity of the bed materials calculated using XRF, TGA and XRD data.

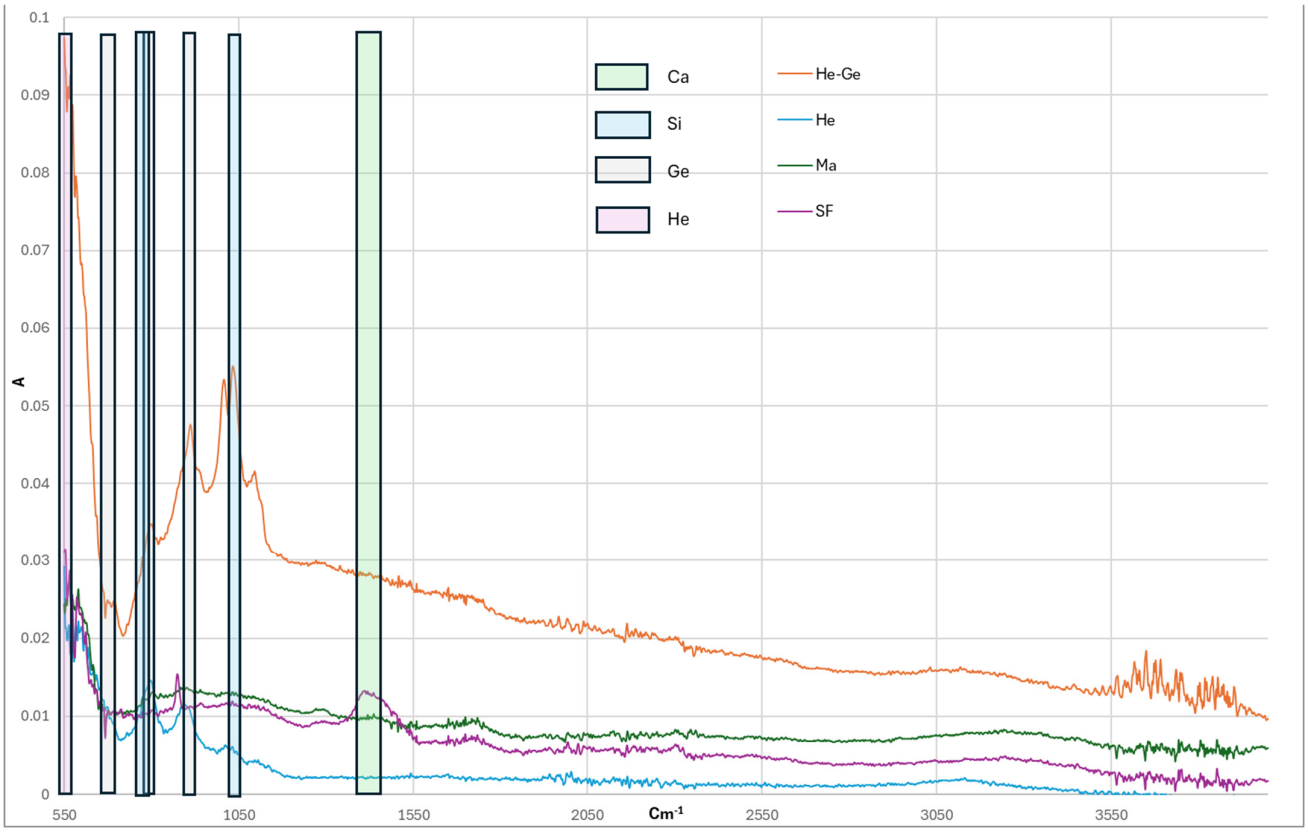

Figure 7. FTIR spectrum of the bed materials with the wavenumber ranges of key bonds highlighted. Orange = hematite–goethite, light blue = hematite, green = magnetite and purple = sinter fines.

7.2. Effect of Biocarbon

The sinter used for these experiments was made with increasing quantities of a 30% biomass fuel. The replacement of fossil carbon with biocarbon was shown to not negatively affect the thermal properties of the sinter, with the emissivity only varying by 3.5% between the samples [42]. The data from this study indicated that the presence of ecoke in the

formation of the sinter does not have a noticeable impact on the quantity of energy absorbed by the bed materials (Figure 8). Therefore, in this analysis, the results are an average of five runs at each temperature.

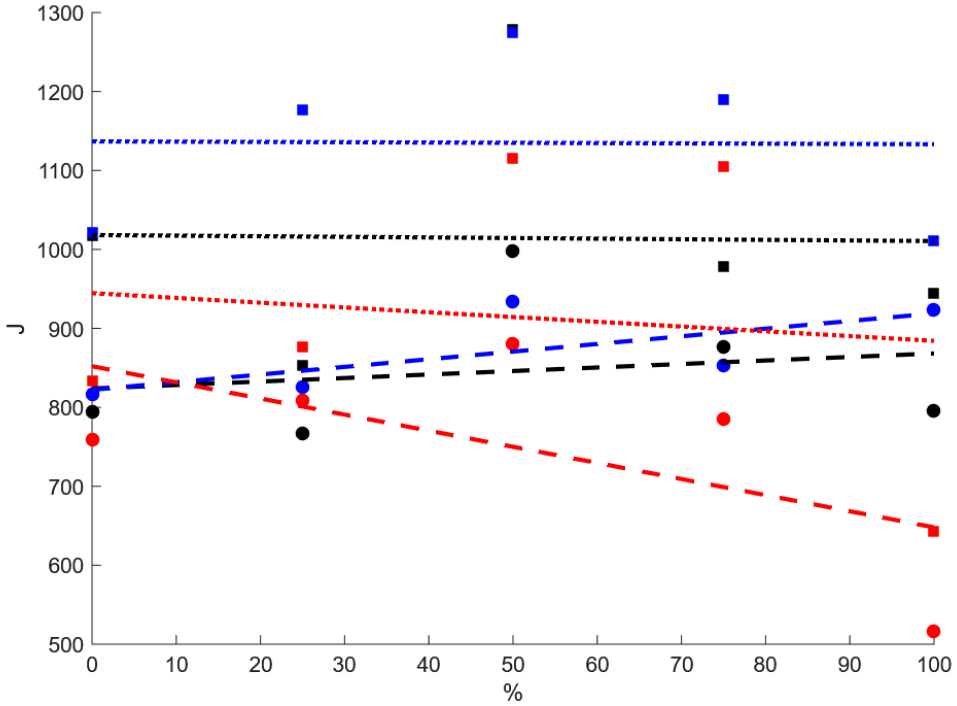

Figure 8. Relationship between the quantity of energy absorbed by the bed materials and the quantity of ecoke used to make the iron ore sinter lumps, where black = 500 °C, blue = 550 °C and red = 600 °C; dotted + squares = top layer and dashed + circles = bottom layer.

7.3. Temperature Results

The magnetite concentrate was an evenly distributed powder with a D_{av} = 0.16 mm (Table 1). At 500 °C, the magnetite concentrate reached an average peak temperature of 74 and 68 °C for the bottom and top layers at a rate of 0.13 and 0.17 °C/s, respectively (Figure 9). The resultant cooling rate was 4.29 and 4.53 times lower than the heating rate for the bottom and top layers. Increasing the temperature to 550 °C increased the maximum temperature by only 7 °C for the bottom layer, but the top layer increased by 17 °C to 85 °C. The heating rate for both layers also increased, but the heating ratio (heating rate/cooling rate) increased for the bottom layer but decreased for the top layer. Lastly, at 600 °C, the peak temperature was 93 and 97 °C, and the heating ratio was 5.37 and 3.73.

The hematite ore, D_{av} = 0.22 mm, was primarily made up of hematite, with small quantities of other elements (Table 1). At 500 °C, the heating rate for the bottom and top layers was 0.09 °C/s, reaching peak temperatures of 72 and 83 °C (Figure 9). Increasing the lump sample temperature to 550 °C resulted in peak temperatures rising to 77 and 91 °C. The resulting heating ratios for the bottom and top layers were 4.93 and 3.2. At 600 °C, the peak temperatures rose to 80 and 96 °C in the bottom and top layers. There was also an inversion in the heating ratio to 3.89 and 4.14.

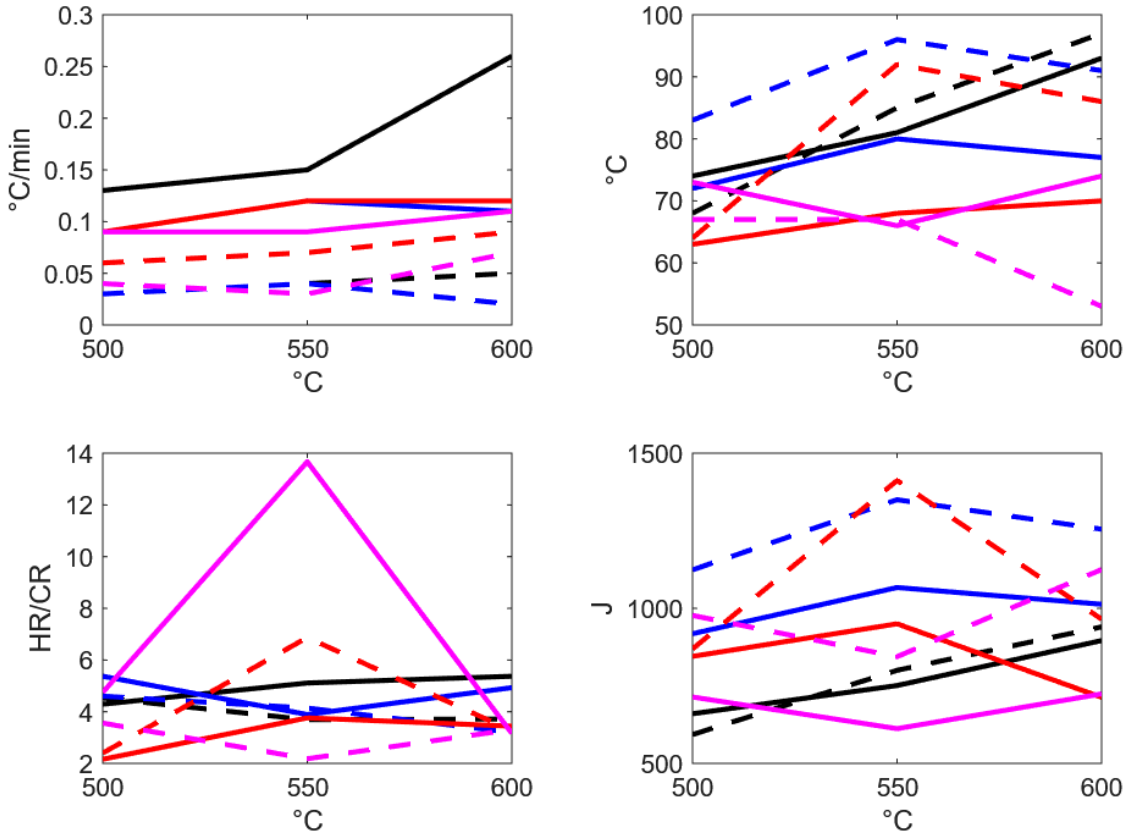

Figure 9. The results of the packed bed experiments using the thermographic data analysed using FLIR Research Studio, where solid lines = bottom layer and dotted lines = top layer; black = magnetite, blue = hematite, red = hematite–goethite and magenta = sinter; clockwise: average heating rate (HR), maximum temperature, heating to cooling ratio (HR/CR) and energy absorbed.

The last ore, the hematite–goethite ore, was a mixture of hematite and goethite, D_{av} = 0.27 mm (Table 1). At 500 °C, it reached an average peak temperature of 63 and 64 °C for the bottom and top layers at a rate of 0.09 °C/s (Figure 9). The resultant cooling rate was 2.16 and 2.40 times lower than the heating rate for the bottom and top layers. Increasing the temperature to 550 °C increased the maximum temperature by only 5 °C for the bottom layer, but the top layer increased by 28 °C to 92 °C. Lastly, at 600 °C, the peak temperature was 70 and 86 °C, and the heating ratio was 3.44 and 3.26.

The sinter fines were a complex mixture of iron oxides and SFCA structures, with the largest average particle size at 2.65 mm (Table 1). At 500 °C, the heating rates were 0.09 and 0.06 °C/s, reaching peak temperatures of 66 and 83 °C (Figure 9). Increasing the lump sample temperature to 550 °C resulted in peak temperatures rising to 73 and 93 °C. The resulting heating ratio for the bottom and top layers was 4.75 and 3.56. At 600 °C, the peak temperature rose to 74 and 104 °C in the bottom and top layers.

7.4. Transfer Dynamics

The distribution of temperatures in the bed materials had a positive correlation with lump sinter temperature, but their chemistry, size distribution and thermal properties affected the overall effectiveness. To be effective, the bed materials needed to quickly absorb the large quantities of thermal energy being radiated out of the lump sinter and then slowly release. The distribution of maximum temperatures between the layers was interesting, as the hematite ore reached the highest temperatures in the 500 °C and 550 °C runs with the magnetite concentrate overtaking in the 600 °C run, whereas in the bottom layer, the hematite ore initially had the highest temperature, 500 °C and 550 °C, but as lump

sinter temperature increased to 600 °C, the sinter fines achieved the highest temperature. There was clearly a difference in the heat transfer dynamics of the two layers, which is further shown by difference in temperature range for the top, 40 °C (38%), and bottom, 30 °C (32%). For a given mass of lump sinter at the sinter to bed material ratio (1:4), the temperature rise per g was highest in the hematite–goethite ore, with a maximum value of 14 °C/g. The other bed materials had a per g rise between 7 and 9 °C/g. Using the heat capacity values of the lump sinter and bed materials in Figures 5 and 6, their resultant thermal energy was calculated (E_L and E_b, respectively) and the thermal efficiency (δ) of each bed material with increasing lump temperature calculated using Equation (8).

$$\delta = 1 - \left(\frac{E_L - E_b}{E_L}\right) \quad (8)$$

At 600 °C, the lump sinter had absorbed between 5.0 and 7.9 kJ of thermal energy from the furnace of which a percentage was lost in the transition from the furnace. The heat transfer through the bottom layer was slower than the top layer due to the higher surface area of the top layer of the bed material in contact with the lump sinter. Figure 10 shows the efficiency calculated based on energy absorption from both layers of each bed material. It was clear that the hematite ore and the hematite–goethite ore had superior overall efficiency compared to the sinter fines and the magnetite concentrate. Interestingly, both the hematite ore and the hematite–goethite ore efficiency reduced at increasing temperature, with the hematite–goethite ore dropping by 11% over the temperature range. Comparatively, the magnetite concentrate had a steadily increasing efficiency, despite being lower than the hematite ore. This could be related to the type of heat transfer occurring in the bed. Evaluating per layer efficiency, the magnetite concentrate was much more consistent over the bottom and top layers compared to the hematite ore, showing a more even coverage and density throughout the bed. The sinter fines were less efficient than the ores due to their higher particle size and low density creating insulating air pockets between the particles, which will be discussed in more detail later. During the experiment, the best performing bed material, the hematite–goethite ore, absorbed a maximum of 2.36 kJ at a lump sinter temperature of 550 °C, whereas the sinter fines absorbed 2.06 kJ at 600 °C.

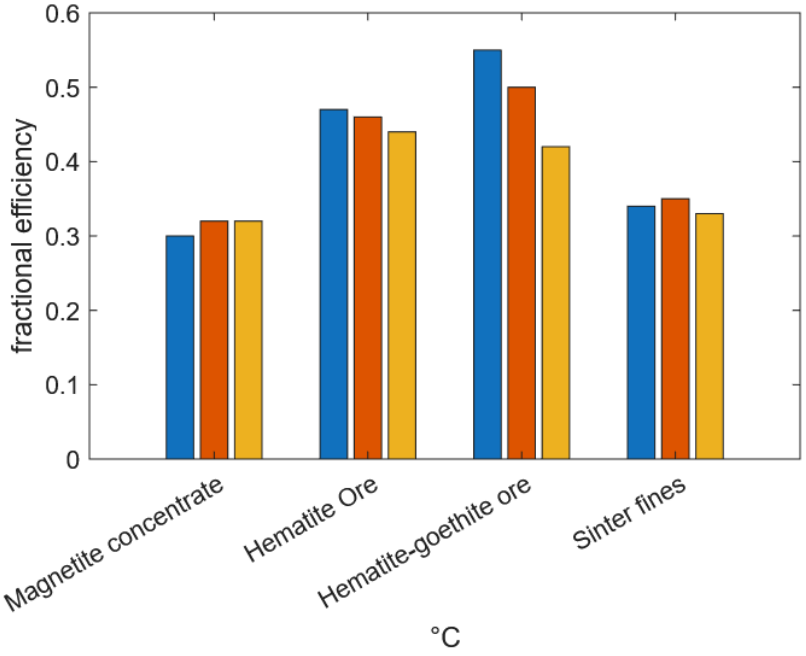

Figure 10. The energy efficiency of each bed material where blue = 500 °C, orange = 550 °C and yellow = 600 °C.

7.5. Heat Flow Tracking

Once in the reactor, the thermal energy was transferred from the lump sinter through the bed via radiation and conduction, forming a heat front that was analysed using image analysis from the thermal camera data. Mathematical models [43,63] have previously been used to predict the effect of different heat transfer modes on the effective thermal conductivity (ETC) of solid beds. The models predicted that an increase in particle size, and therefore voidage, would lead to a reduced effective thermal conductivity because of the low thermal conductivity of air, although the use of high-emissivity materials, such as iron oxide, could counteract this by means of an increased photon count moving through the voids (Figure 1).

Radiation from a material is controlled by its emissivity, surface area and temperature, as described in the Stefan–Boltzman equation, Equation (9).

$$Q = \epsilon \sigma A T^4 \tag{9}$$

As emissivity and temperature increase, more energy is emitted as infrared radiation, with flux (Q) increasing by the fourth power of absolute temperature. In Figure 7, the polar bonds within the bed materials were identified using Fourier transform infrared spectroscopy: Fe-O, O-H, Ca-O and Si-O, whereas the air contained in the pores is 78% N_2, which is a poor absorber of infrared radiation. Conductive processes are controlled by the thermal conductivity (k), thermal diffusivity (D) and heat capacity (C_p). Thermal conductivity describes the rate of heat flow across a temperature gradient, where a high k can move heat quickly and a low k is a barrier to heat flow. Diffusivity describes the temperature change during conduction, where a high D shows that heat is dissipated and has a lower rate of temperature increase. Finally, a high heat capacity describes the energy input required to increase the temperature by one °C.

The bed materials have a thermal conductivity of 1.5–5.98 W/mK and thermal diffusivities of 2.2×10^{-6}–5.8×10^{-6} m^2/s, whereas air has a thermal conductivity of 0.024 W/mK and a thermal diffusivity of 1.9×10^{-5} m^2/s. Figure 11 shows how energy moves from sinter, through a pore and into the bed material, taking into account the infrared and conductive properties of each material. Figure 12 shows how energy is transferred through direct conduction from the lump sinter to the bed material; the thermal conductivity of both materials is similar, allowing temperature to flow quickly across the boundary. Preferential conduction through the bed materials causes conduction around pores, creating tendrils in the image analysis. The emissivity of the bed materials is also high (Table 5), allowing the bed materials to radiate through pores and heat neighbouring bed materials. The difference in thermal properties of lump sinter, air and the bed materials show how isolated hotspots in the image analysis (Figure 13) from the bed material heats faster than the air in the pore.

Figure 13 shows how the bed materials pack based on particle morphologies in the scanning electron microscope images (Figure 2).

The maximum recorded temperature was found to correlate well with the heat capacity of the bed materials; a lower heat capacity resulted in faster conduction (Figure S3). Numerical models predicted that an increase in voidage would result in a more resistive bed and therefore a lower heating rate, which was seen in both layers but to a lesser extent in the top. Because of the high emissivity of the bed materials (Table 5), a high proportion of the heat could be transferred through radiation through a very porous bed.

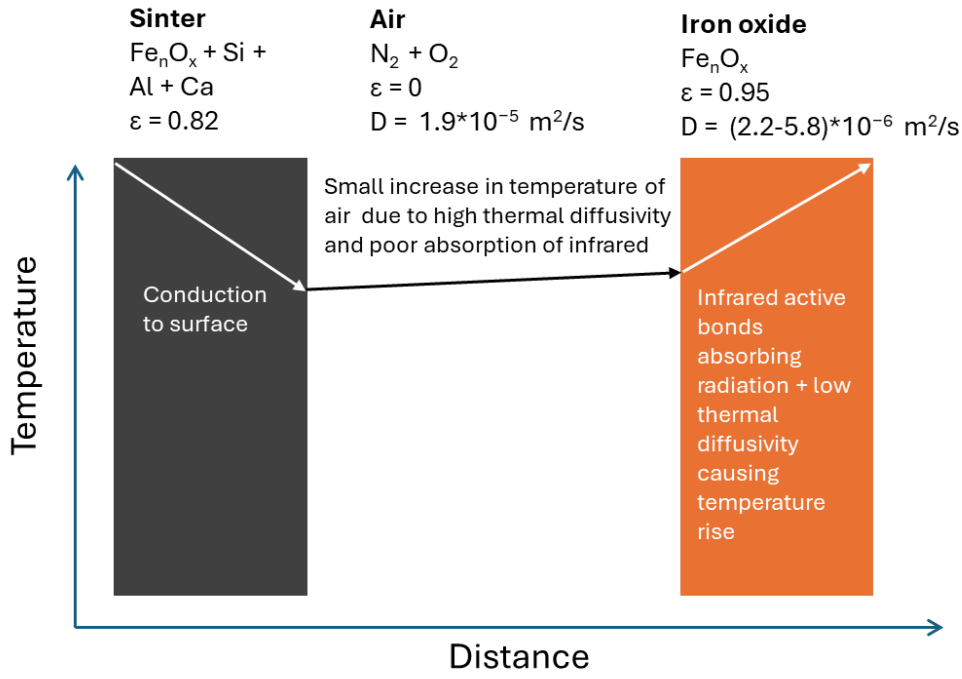

Figure 11. Model of heat transfer though a pore with the bed material.

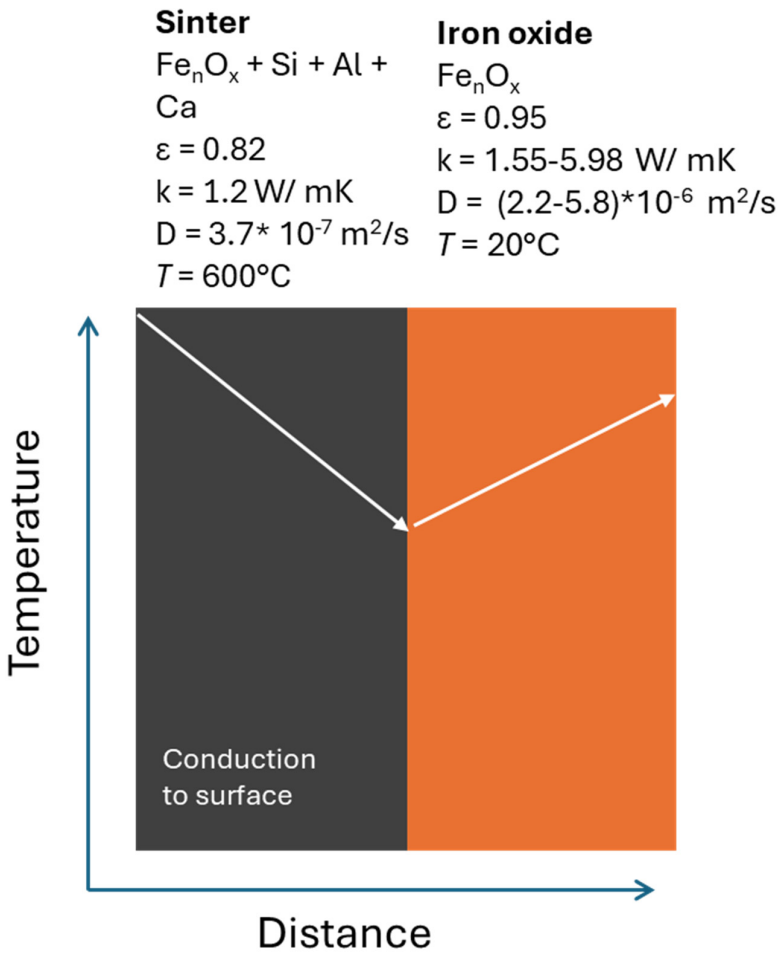

Figure 12. Model of heat transfer from lump sinter into the bed material.

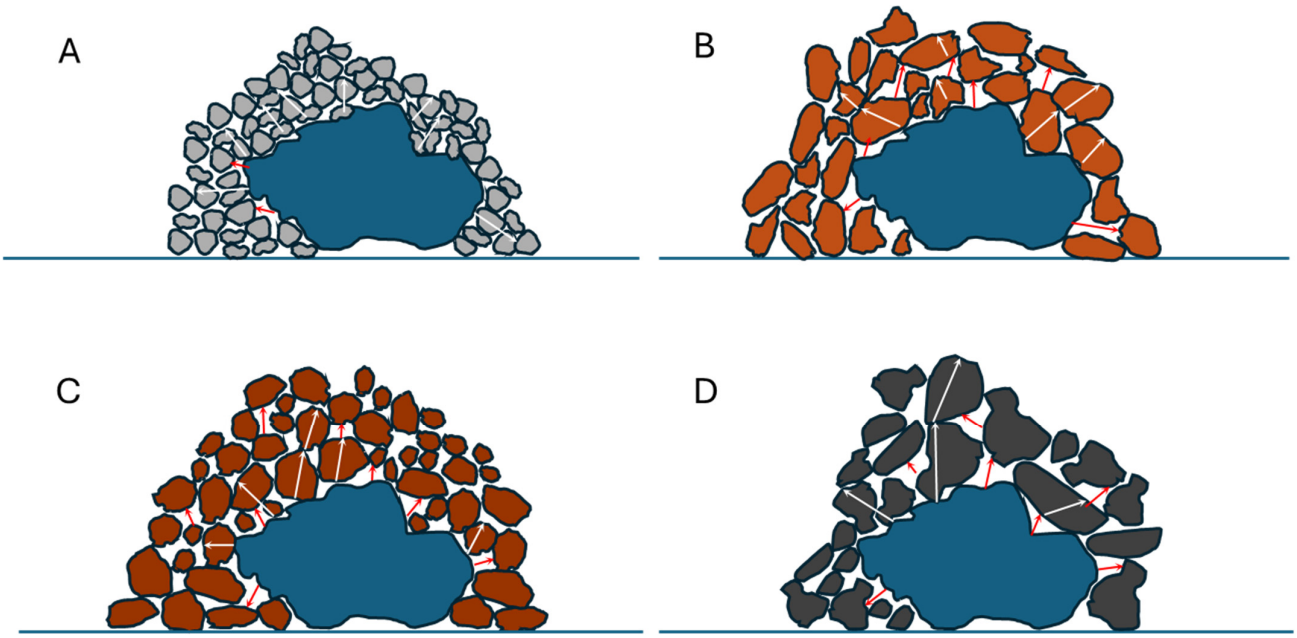

Figure 13. Model of bed packing and the associated heat transfer modes in the bed materials where (**A**) = Magnetite concentrate, (**B**) = Hematite Ore, (**C**) = Hematite-goethite ore, (**D**) = Sinter Fines, where radiation = red arrows and conduction = white arrows.

Figure 14 shows the results of the image analysis of how the heat movement through the bed differed in each bed material. Panel A depicted the smooth flow of heat from the lump sinter through the top layer of the magnetite concentrate, D_{av} = 0.16 mm. The steadily increasing distribution of the areas (Figure 15) further indicated that heat was transferred smoothly through direct conduction. Additionally, the presence of very few heat spots due to the high bed density, 999.3 kg/m^3, leads to very few voids through which energy could be transferred by radiation. These image-based results correlate with the BET and SEM analysis (Table 2 and Figure 2), where beds with higher surface areas but moderate pore volumes (e.g., hematite–goethite) showed distributed and persistent heat fronts, while the sinter fines, with both high voidage and pore volume, exhibited delayed heat propagation and more fragmented thermal fronts. The magnetite concentrate had the highest thresholded area after 2 min, which correlates with its high thermal conductivity (Table 4).

Figure 14. Thermal images taken every 10 s for the first 2 min of heating at 550 °C thresholded using ImageJ at a greyscale value corresponding to 60 °C, where (**A**) = the magnetite concentrates, (**B**) = the hematite ore, (**C**) = the hematite–goethite ore and (**D**) = sinter fines.

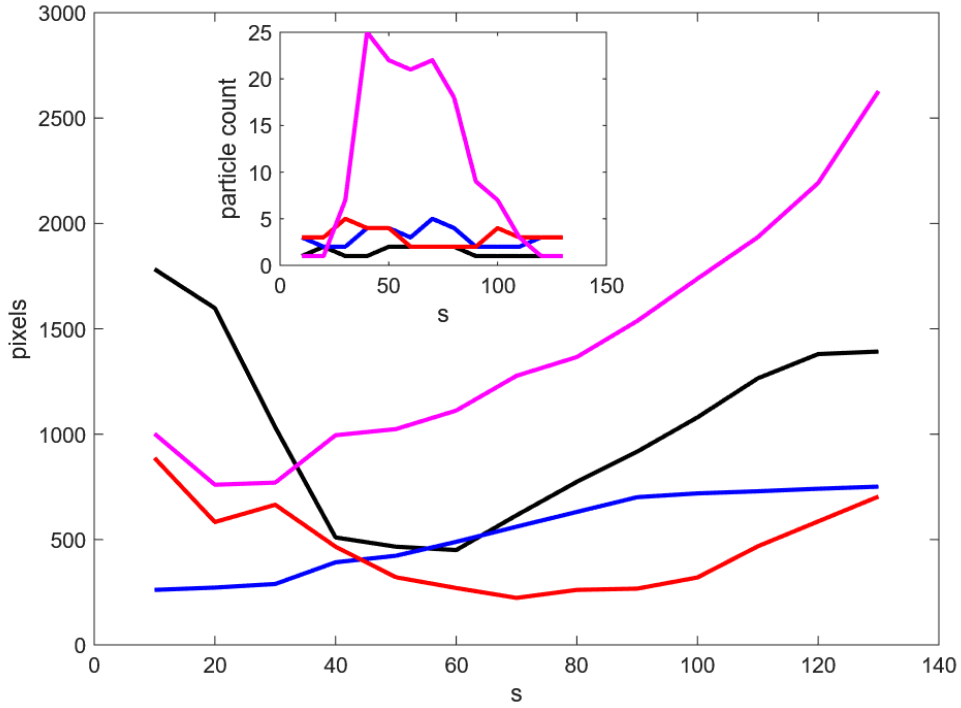

Figure 15. The total area (main) and number of particles (insert) calculated through image analysis for the 500 °C runs, where black = magnetite, blue = hematite, red = hematite–goethite and magenta = sinter fines.

Conversely, bed materials the hematite ore and hematite–goethite ore had a slightly larger D_{av} = 0.22 and 0.27 mm but a wider particle distribution, thus forming a less dense bed with a higher proportion of voids (Figure 1). The thermal conductivity of the hematite ore was lower compared to the other ores, thus reducing the ratio of conduction to radiation. The images in panels B and C showed slower and more uneven heat flow, as pores impeded the energy flow and areas of small particles acted as conducting bridges to larger particles. This process is visualised in Figure 15, where the hematite ore has a slower increase in area than the magnetite concentrate and an increased breaking of the heat front. The hematite–goethite ore had a high initial area that steadily decreased but recovered to a similar final area to the hematite ore. The decreasing area could be explained by an initial heating of the small particles, which then transferred to the wider bed. Lastly, the sinter fines, D_{av} = 2.65, ρ = 791.9 kg/m^3, had a very high proportion of voids within the bed (Figure 1). Figure 14 shows that individual particles in contact with the lump sinter increased in temperature via conduction before then radiating their energy through the pores, a large number of hot spots (Figure 14), transferring energy from particle to particle while slowly heating the air increasing the total area and reducing the number of spots as the temperature becomes more homogeneous. The heating rate data (Figure 9) shows that the magnetite concentrate had a consistently high heating rate, while the sinter fines had a consistently low value. The magnetite concentrates and the hematite ore varied throughout the tests due to the more inconsistent packing arrangements caused by the wider particle size distribution seen in the optical and SEM images (Figures 1 and 2). For the most efficient heat transfer, a smaller particle size reduced pore volume and increased the contact area between the bed material and lump sinter, facilitating rapid conductive heat transfer. The BET and surface area (Table 2) and pore volume data confirm these findings. Materials with higher surface area had a stronger interaction with radiative heat transfer because of higher IR-active surface exposure, but excessive pore volume introduced insulating voids, lowering conduction efficiency. For example, the hematite–goethite ore had a high surface area but moderate

pore volume, balancing radiative absorption and conductive heat transfer. Analysing the 600 °C runs resulted in a similar heat flow pattern for each bed material with a faster rate, which correlates with the heating rate data. Figures S4–S7 present the difference in the heat flow between the 550 °C runs and the 500 °C and 600 °C runs for the hematite ore and the hematite–goethite ore, respectively. As the temperature increased to 600 °C, the flow became more stable, showing fewer hotspots and a smoother increase in area over the first 2 min. While the increase in the quantity of biofuel being used to make the sinter had a negative effect on its heat capacity (Figure 5), it was found that the rate limiting step was the absorption of energy by the bed material. Figure S8 shows that the increase in the percentage of ecoke in the sinter mixture had little to no correlation with the average peak temperatures for all the bed materials, indicating that the choice of bed material had a greater impact. This further validates the use of hybrid biofuel as an effective sustainable replacement for coke breeze.

The area under the temperature curve (Figure 16) was a secondary indicator of the effectiveness of the bed material at absorbing and, more importantly, retaining energy. The magnetite concentrate and the hematite–goethite ore were the most consistent at absorbing energy over the entire range of temperatures, whereas the hematite ore and the sinter fines fluctuated more because of their wider size distribution. In most cases, the top layer had a larger area due to the higher maximum temperatures reached because of the higher contact area with the lump sinter, although the slower cooling rate of the bottom layer increased the area reducing the difference. Overall, the hematite–goethite ore had the lowest area, and the hematite ore and the magnetite concentrate had the largest. In the energy balance, the heat capacity of both the sinter and the bed material were considered, meaning that the magnetite concentrate became much more like the sinter fines and the hematite ore to the hematite–goethite ore.

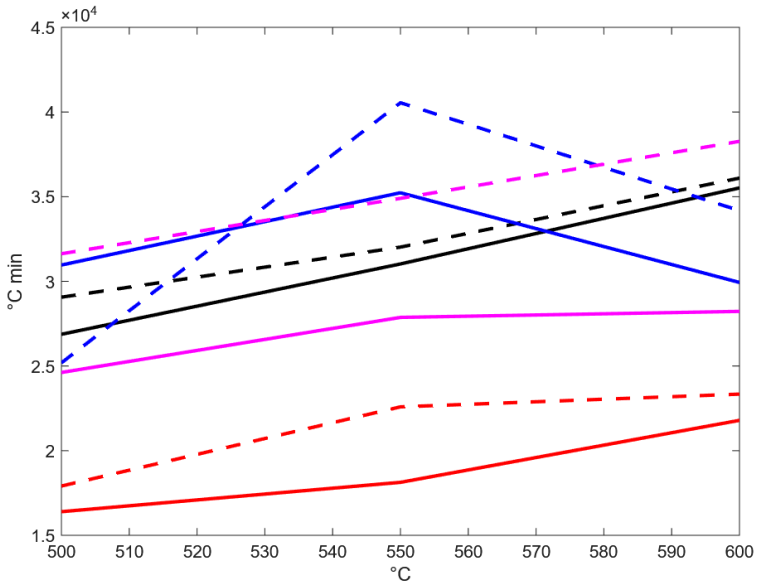

Figure 16. Area under the temperature curves, where solid lines = bottom layer and dotted lines = top layer; black = magnetite, blue = hematite, red = hematite–goethite and magenta = sinter.

The high heat capacity of the hydrated goethite ore (Figure 6) combined with the higher temperature efficiency of the magnetite concentrate (Figure 10) would form an optimised chemistry for absorbing thermal energy. Image analysis identified the pores created by the wide size distribution of the goethite ore slowed the rate of heat transfer because of the reduced thermal conductivity of air. Therefore, the secondary addition of magnetite concentrate into a goethite bed would reduce the volume of insulating air

within the bed, increasing the rate of heat transfer and overall efficiency. Together, the data show that the chemistry of the hematite–goethite ore, i.e., quantity of FeOOH, and the particle size distribution of the magnetite concentrate would, if combined, create a very effective bed material for absorbing excess thermal energy from iron ore sinter. The absorption of energy by the bed material before sintering will result in a lower quantity of energy required to melt the raw mixture, reducing the required fuel rate. Using the calorific content of the fuel mixture, measured by bomb calorimetry [64], the theoretical percentage fuel saving for each bed material was calculated. Unsurprisingly, the hematite ore had the highest fuel saving, with 0.16 kg of fuel saved per 0.885 kg used in the sinter pot. Scaled up, this is a saving of 9.4 kg per tonne of fuel (Figure S9). Despite having the lowest transfer efficiency, the sinter fines still had a potential saving of 1.1 kg/tonne. In comparison to moving grates and vertical tanks, this new method directly transfers heat into the sinter bed instead of using an intermediate transfer fluid, thus reducing the effect of transfer loss. During the experiment, cooling rates of 1.3–4.2 °C/min were achieved, which is the ideal range for efficient formation of SFCA [18]. The most efficient bed material, the hematite–goethite ore, absorbed 2.36 kJ of energy over 328 s from 10 g of sinter. Scaled up to a rate of 9300 tonne/h of sinter, this results in a heat utilisation of 2.194×10^9 kJ/h. Studies on the moving grate style air cooled simulations by Zhang et al. [65] had a waste heat utilization of 2.55×10^8 kJ/h, and simulations by Liu et al. [28] were at 1.90×10^8 kJ/h. However, the vertical tank arrangement had a heat utilisation of 1.49×10^8 kJ/h [37], showing little improvement compared to the moving grate process. Lastly, the solid–solid process model by Felinks et al. [39] had predicted recoveries of 70% over multiple steps and 50% over two steps, similar to the efficiency data in Figure 10. Based on a CO_2 emission factor of 2.86 kg CO_2/kg of coke, the projected fuel saving of 9.4 kg/tonne corresponds to ~27 kg CO_2 saved per tonne of sinter.

7.6. Industrial Application

In the industrial iron ore sintering process, at the end of the strand, the iron ore sinter is crushed and size classified. To enter the blast furnace, sinter must be +6.3 mm, creating a hard size cutoff on the cooling strand. In the scaled iron oxide bed process, the bed materials will be added at the start of the cooling strand and then extracted at the peak of energy absorption based on the results in Figure 9, using a 5 mm aperture at the base of the cooling strand. This study used a 4:1 ratio of bed material to lump sinter; in an industrial process, this will equate to 4 tonnes of ore per tonne of sinter, equating to a total bed porosity of 0.88 in the quartz reactor. However, in the industrial process, the bed porosity is 0.3–0.5 [66], reducing the quantity of bed material in the cooling strand by 58%. The capital expenditure of the proposed process would be the installation of new conveyor equipment and sieves to transport and extract the bed material to and from the cooling strand. Operational costs would include the running of the conveyors but would reduce due to the coke rate reducing by 9.4 kg/tonne.

8. Conclusions

The developments in technology for recovering heat from iron ore sinter has not considered the infrared absorption capability of iron oxides, instead focusing on adapting the air driven process. This experimental method was developed to provide a resource-efficient and repeatable platform to identify efficient solid heat transfer materials for the recovery of energy from the iron ore sintering process. The use of quartz glass to quantify the type of heat flow through the bed was inspired by tests investigating the flame front in the sintering processes [2].

Preliminary FTIR measurements demonstrated that the interaction of the chosen bed materials with infrared radiation was significant and corroborated the increased efficiency of iron hydroxides instead of air as heat transfer material. The BET surface area and porosity data provided evidence for how internal structure governs energy absorption and retention, further validating the experimental model. Comparison of the dynamics of each bed using infrared thermography and image analysis found that the bulk bed density and surface area impacted the ratio of conduction to radiation, whereas the chemical composition controlled the rate and quantity of infrared radiation absorbed. The fine evenly distributed magnetite concentrate transferred energy through smooth conduction, whereas the larger, widely distributed sinter fines had a more separated profile, indicating radiative transfer, although both had a reduced efficiency compared to the hematite–goethite ore which transferred energy through a mixture of radiation and conduction. The hydrated fraction contributed to the highest thermal efficiency absorbing 2.36×10^5 KJ/T, equivalent to 9.4 kg/T of fossil fuel. The BET surface area and porosity data confirmed that internal surface topology and pore volume significantly affect energy absorption and retention. Future work will assess the reusability of the bed materials under industrial cycling conditions and optimise composite formulations, combining high surface area and low voidage.

Supplementary Materials: The following supporting information can be downloaded at: https://www.mdpi.com/article/10.3390/chemengineering9060118/s1.

Author Contributions: Conceptualisation, S.R. and P.J.H.; methodology S.R.; validation, P.J.H., C.M., S.C. and S.K.; formal analysis, S.R.; investigation, S.R.; resources, Tata Steel; data curation, P.J.H.; writing—original draft preparation, S.R. and S.K.; writing—review and editing, P.J.H., C.M., S.C. and S.K.; visualisation, S.R.; supervision, P.J.H., C.M. and S.C.; funding acquisition, P.J.H. and C.M. All authors have read and agreed to the published version of the manuscript.

Funding: We gratefully thank EPSRC and Tata Steel for cosponsoring an iCASE PhD studentship (Voucher no. 20000176) for SR and EPSRC for funding the Sustain Hub (EP/S018107/1) for PJH.

Data Availability Statement: The original contributions presented in this study are included in the article/Supplementary Material. Further inquiries can be directed to the corresponding author.

Conflicts of Interest: Author Ciaran Martin was employed my Tata Steel Uk Ltd. The remaining authors declare that the research was conducted in the absence of any commercial or financial relationships that could be construed as a potential conflict of interest.

Abbreviations

The following abbreviations are used in this manuscript:

BET	Brunauer–Emmett–Teller
COP21	Conference of the parties 2021
CR	Cooling rate
FEG	Field Emission Gun
FEI	Field Electron and Ion Company
FTIR	Fourier transform infrared spectroscopy
HR	Heating rate
SEM	Scanning electron microscope
SFCA	Silico-ferrite of calcium and aluminium
UN	United nations
XRD	X-ray diffraction
XRF	X-ray fluorescence

References

1. Findorák, R.; Legemza, J.; Fröhlichová, M.; Fabriciová, G.; Džupková, M. New Utilization of Specific Biomass: Lignin in the Iron Ore Sintering Process. *Metals* **2020**, *10*, 1170. [CrossRef]
2. Cheng, Z.L.; Wei, S.S.; Guo, Z.G.; Yang, J.; Wang, Q.W. Improvement of heat pattern and sinter strength at high charcoal proportion by applying ultra-lean gaseous fuel injection in iron ore sintering process. *J. Clean. Prod.* **2017**, *161*, 1374–1384. [CrossRef]
3. Gan, M.; Fan, X.; Ji, Z.; Chen, X.; Jiang, T.; Yu, Z. Effect of distribution of biomass fuel in granules on iron ore sintering and NOx emission. *Ironmak. Steelmak.* **2014**, *41*, 430–434. [CrossRef]
4. Wu, Y.; Gan, M.; Ji, Z.; Fan, X.; Zhao, G.; Zhou, H.; Zheng, H.; Wang, X.; Liu, L.; Li, J. New approach to improve heat energy utilization efficiency in iron ore sintering: Exploration of surface fuel addition. *Process Saf. Environ. Prot.* **2024**, *190*, 125–137. [CrossRef]
5. Zhao, G.; Clarke, J.; Searle, J.; Lewis, R.; Baker, J. Economic analysis of integrating photovoltaics and battery energy storage system in an office building. *Energy Build.* **2023**, *284*, 112885. [CrossRef]
6. Nations, U. Progress Towards the Sustainable Development Goals. 2024. Available online: https://unstats.un.org/sdgs/files/report/2024/SG-SDG-Progress-Report-2024-advanced-unedited-version.pdf (accessed on 15 March 2025).
7. Nations, U. Paris Agreement. 2015. Available online: https://unfccc.int/sites/default/files/english_paris_agreement.pdf (accessed on 15 March 2025).
8. Cheng, Z.; Guo, Z.; Tan, Z.; Yang, J.; Wang, Q. Waste heat recovery from high-temperature solid granular materials: Energy challenges and opportunities. *Renew. Sustain. Energy Rev.* **2019**, *116*, 109428. [CrossRef]
9. Feng, H.; Chen, L.; Liu, X.; Xie, Z.; Sun, F. Constructal optimization of a sinter cooling process based on exergy output maximization. *Appl. Therm. Eng.* **2016**, *96*, 161–166. [CrossRef]
10. de Castro, J.A.; de Oliveira, E.M.; de Campos, M.F.; Takano, C.; Yagi, J.-i. Analyzing cleaner alternatives of solid and gaseous fuels for iron ore sintering in compacts machines. *J. Clean. Prod.* **2018**, *198*, 654–661. [CrossRef]
11. Suopajärvi, H.; Pongrácz, E.; Fabritius, T. The potential of using biomass-based reducing agents in the blast furnace: A review of thermochemical conversion technologies and assessments related to sustainability. *Renew. Sustain. Energy Rev.* **2013**, *25*, 511–528. [CrossRef]
12. Cheng, Z.; Wang, J.; Wei, S.; Guo, Z.; Yang, J.; Wang, Q. Optimization of gaseous fuel injection for saving energy consumption and improving imbalance of heat distribution in iron ore sintering. *Appl. Energy* **2017**, *207*, 230–242. [CrossRef]
13. Oyama, N.; Iwami, N.; Yamamoto, T.; Machida, S.; Higuchi, T.; Sato, M.; Takeda, K.; Watanabe, Y.; Shimizu, M.; Nishioka, K. Development of Secondary-fuel Injection Technology for Energy Reduction in the Iron Ore Sintering Process. *ISIJ Int.* **2011**, *51*, 913–921. [CrossRef]
14. Loo, C.E.; Aboutanios, J. Changes in water distribution when sintering porous goethitic iron ores. *Miner. Process. Extr. Metall.* **2000**, *109*, 23–35. [CrossRef]
15. Geerdes, M.; Chaigneau, R.; Lingiardi, O.; Molenaar, R.; Van Opbergen, R.; Yongzhi, S.; Warren, P. *Modern Blast Furance Ironmaking: An Introduction*; IOS Press BV: Amsterdam, The Netherlands, 2020.
16. Webster, N.A.S.; Pownceby, M.I.; Madsen, I.C.; Studer, A.J.; Manuel, J.R.; Kimpton, J.A. Fundamentals of Silico-Ferrite of Calcium and Aluminum (SFCA) and SFCA-I Iron Ore Sinter Bonding Phase Formation: Effects of CaO:SiO_2 Ratio. *Metall. Mater. Trans. B* **2014**, *45*, 2097–2105. [CrossRef]
17. Nicol, S.; Chen, J.; Pownceby, M.I.; Webster, N.A.S. A Review of the Chemistry, Structure and Formation Conditions of Silico-Ferrite of Calcium and Aluminum ('SFCA') Phases. *ISIJ Int.* **2018**, *58*, 2157–2172. [CrossRef]
18. Hsieh, L.; Whiteman, J.A. Effect of Raw Material Composition on the Mineral Phases in Lime-fluxed Iron Ore Sinter. *ISIJ Int.* **1993**, *33*, 462–473. [CrossRef]
19. Caputo, A.C.; Pelagagge, P.A. Heat recovery from moving cooling beds: Transient modeling by dynamic simulation. *Appl. Therm. Eng.* **1999**, *19*, 21–35. [CrossRef]
20. Pelagagge, P.M.; Caputo, A.C.; Cardarelli, G. Optimization criteria of heat recovery from solid beds. *Appl. Therm. Eng.* **1997**, *17*, 57–64. [CrossRef]
21. He, K.; Wang, L. A review of energy use and energy-efficient technologies for the iron and steel industry. *Renew. Sustain. Energy Rev.* **2017**, *70*, 1022–1039. [CrossRef]
22. Tanaka, N. Waste Heat Recovery from Sintering Plants. *Trans. Iron Steel Inst. Jpn.* **1980**, *20*, 200–203. [CrossRef]
23. Pardo, N.; Moya, J.A. Prospective scenarios on energy efficiency and CO_2 emissions in the European Iron & Steel industry. *JRC Sci. Policy Rep. Eur. Comm.* **2012**, *54*, 113–128. [CrossRef]
24. Brewer, P.G.; Peltzer, E.T. The Molecular Basis for the Heat Capacity and Thermal Expansion of Natural Waters. *Geophys. Res. Lett.* **2019**, *46*, 13227–13233. [CrossRef]
25. Qin, S.; Chang, S. Modeling, thermodynamic and techno-economic analysis of coke production process with waste heat recovery. *Energy* **2017**, *141*, 435–450. [CrossRef]

26. Grace, J.R. Contacting modes and behaviour classification of gas—Solid and other two-phase suspensions. *Can. J. Chem. Eng.* **1986**, *64*, 353–363. [CrossRef]
27. Wen, Z.; Shi, H.Z.; Zhang, X.; Lou, G.F.; Liu, X.L.; Dou, R.F.; Su, F.Y. Numerical simulation and parameters optimization on gas–solid heat transfer process of high temperature sinter. *Ironmak. Steelmak.* **2011**, *38*, 525–529. [CrossRef]
28. Liu, Y.; Yang, J.; Wang, J.; Cheng, Z.L.; Wang, Q.W. Energy and exergy analysis for waste heat cascade utilization in sinter cooling bed. *Energy* **2014**, *67*, 370–380. [CrossRef]
29. Jang, J.-Y.; Chiu, Y.-W. 3-D Transient conjugated heat transfer and fluid flow analysis for the cooling process of sintered bed. *Appl. Therm. Eng.* **2009**, *29*, 2895–2903. [CrossRef]
30. Sun, K.; Tseng, C.-T.; Shan-Hill Wong, D.; Shieh, S.-S.; Jang, S.-S.; Kang, J.-L.; Hsieh, W.-D. Model predictive control for improving waste heat recovery in coke dry quenching processes. *Energy* **2015**, *80*, 275–283. [CrossRef]
31. Dong, H.; Li, L.; Lie, W.; Wang, B.; Suo, Y.; Cai, J. Process of Waste Heat Recovery and Utilization for Sinter in Vertical Tank. *China Metall.* **2012**, *22*, 6–11.
32. Dong, H.; Zhao, Y.; Cai, J.J.; Zhou, J.W.; Ma, G.Y. On the air leakage problem in sintering cooling system. *Kang T'ieh/Iron Steel* **2012**, *47*, 95–99.
33. Feng, J.; Dong, H.; Dong, H. Modification of Ergun's correlation in vertical tank for sinter waste heat recovery. *Powder Technol.* **2015**, *280*, 89–93. [CrossRef]
34. Feng, J.; Dong, H.; Gao, J.; Li, H.; Liu, J. Numerical investigation of gas-solid heat transfer process in vertical tank for sinter waste heat recovery. *Appl. Therm. Eng.* **2016**, *107*, 135–143. [CrossRef]
35. Feng, J.; Dong, H.; Gao, J.; Liu, J.; Liang, K. Exergy transfer characteristics of gas-solid heat transfer through sinter bed layer in vertical tank. *Energy* **2016**, *111*, 154–164. [CrossRef]
36. Feng, J.; Dong, H.; Liu, J.; Liang, K.; Gao, J. Experimental study of gas flow characteristics in vertical tank for sinter waste heat recovery. *Appl. Therm. Eng.* **2015**, *91*, 73–79. [CrossRef]
37. Feng, J.; Zhao, L.; Zhang, S.; Dong, H. Exergy analysis and parameter optimization of sinter cooling process in vertical moving bed for waste heat recovery. *Appl. Therm. Eng.* **2020**, *175*, 115370. [CrossRef]
38. Zhang, S.; Zhao, L.; Feng, J.; Luo, X.; Dong, H. Thermal analysis of sinter vertical cooler based on waste heat recovery. *Appl. Therm. Eng.* **2019**, *157*, 113708. [CrossRef]
39. Felinks, J.; Brendelberger, S.; Roeb, M.; Sattler, C.; Pitz-Paal, R. Heat recovery concept for thermochemical processes using a solid heat transfer medium. *Appl. Therm. Eng.* **2014**, *73*, 1006–1013. [CrossRef]
40. Brunetti, M.; Prodi, F. The climate system. *EPJ Web Conf.* **2015**, *98*, 02001. [CrossRef]
41. Namduri, H.; Nasrazadani, S. Quantitative analysis of iron oxides using Fourier transform infrared spectrophotometry. *Corros. Sci.* **2008**, *50*, 2493–2497. [CrossRef]
42. Reis, S.; Holliman, P.J.; Martin, C. Evaluation of the effect of a biomass fuel source on the thermal properties of iron ore sinter. *Fuel* **2025**, *381*, 133172. [CrossRef]
43. Tsory, T.; Ben-Jacob, N.; Brosh, T.; Levy, A. Thermal DEM–CFD modeling and simulation of heat transfer through packed bed. *Powder Technol.* **2013**, *244*, 52–60. [CrossRef]
44. Bhagat, R.P.; Chattoraj, U.S.; Sil, S.K. Porosity of Sinter and Its Relation with the Sintering Indices. *ISIJ Int.* **2006**, *46*, 1728–1730. [CrossRef]
45. Tian, Y.; Song, S.; Xu, X.; Wei, X.; Yan, S.; Zhan, M. Study on Fluidization Characteristics of Magnetically Fluidized Beds for Microfine Particles. *Minerals* **2022**, *12*, 61. [CrossRef]
46. Motta, E.; Moraes, I.; Apolônio, P.; Ribeiro, D.; Cunha, E. Incorporating mineralogical and density parameters in ferrous resource evaluation using mineralogical norm calculation-MNC. In Proceedings of the 24th World Mining Congress, Rio de Janeiro, Brazil, 21 October 2016; pp. 210–221.
47. Malcolm, W.; Chase, J. *NIST-JANAF Themochemical Tables*, 4th ed.; American Chemical Society: Washington, DC, USA, 1998.
48. Zöll, K.; Benisek, A.; Dachs, E.; Kahlenberg, V.; Saxer, A.; Tropper, P.; de Villiers, J. Stability and calorimetric studies of silico-ferrites of calcium aluminum and magnesium. *J. Am. Ceram. Soc.* **2018**, *101*, 4193–4202. [CrossRef]
49. Li, Y.; Zeng, J.; Zhang, N.; Xue, Y.; Hou, Y.; Lv, X. Preparation, Structure, and Characterization of SFCA-I. In Proceedings of the TMS 2024 153rd Annual Meeting & Exhibition Supplemental Proceedings, Orlando, FL, USA, 7 February 2024; Springer Nature: Cham, Switzerland; pp. 1836–1845. [CrossRef]
50. Lai, Z.; Zhou, H.; Zhou, M.; Lv, L.; Meng, H.; Cen, K. Experimental study on storage performance of packed bed solar thermal energy storage system using sintered ore particles. *Sol. Energy Mater. Sol. Cells* **2022**, *238*, 111654. [CrossRef]
51. Lorente, E.; Peña, J.A.; Herguido, J. Separation and storage of hydrogen by steam-iron process: Effect of added metals upon hydrogen release and solid stability. *J. Power Sources* **2009**, *192*, 224–229. [CrossRef]
52. Lorente, E.; Peña, J.A.; Herguido, J. Cycle behaviour of iron ores in the steam-iron process. *Int. J. Hydrog. Energy* **2011**, *36*, 7043–7050. [CrossRef]

53. Peña, J.A.; Lorente, E.; Romero, E.; Herguido, J. Kinetic study of the redox process for storing hydrogen: Reduction stage. *Catal. Today* **2006**, *116*, 439–444. [CrossRef]
54. Nandiyanto, A.B.D.; Ragadhita, R.; Fiandini, M.; Husaeni, D.N.A.; Aziz, M. The Role of Iron Oxide in Hydrogen Production: Theory and Bibliometric Analyses. *Moroc. J. Chem.* **2023**, *11*, 897–1318. [CrossRef]
55. Otsuka, K.; Yamada, C.; Kaburagi, T.; Takenaka, S. Hydrogen storage and production by redox of iron oxide for polymer electrolyte fuel cell vehicles. *Int. J. Hydrog. Energy* **2003**, *28*, 335–342. [CrossRef]
56. Huang, X.B.; Lv, X.W.; Bai, C.G.; Qiu, G.B.; Lu, L. Effect of pre-wetting treatment on the granulation behavior of iron ore fines. *ISIJ Int.* **2014**, *54*, 2721–2727. [CrossRef]
57. Gan, M.; Fan, X.H.; Ji, Z.Y.; Chen, X.L.; Yin, L.; Jiang, T.; Yu, Z.Y.; Huang, Y.S. Optimising method for improving granulation effectiveness of iron ore sintering mixture. *Ironmak. Steelmak.* **2015**, *42*, 351–357. [CrossRef]
58. Fu, T.; Tan, P.; Zhong, M. Experimental research on the influence of surface conditions on the total hemispherical emissivity of iron-based alloys. *Exp. Therm. Fluid Sci.* **2012**, *40*, 159–167. [CrossRef]
59. Harvey, T. Influence of Mineralogy and Pore Structure on the Reducibility and Strength of Iron Ore Sinter. Ph.D. Thesis, University of Newcastle Australia, Newcastle, Australia, 2020.
60. Kim, D.; Townsley, S.; Grassian, V.H. Vibrational spectroscopy as a probe of heterogeneities within geochemical thin films on macro, micro, and nanoscales. *RSC Adv.* **2023**, *13*, 28873–28884. [CrossRef] [PubMed]
61. Baabu, P.R.S.; Kumar, H.K.; Gumpu, M.B.; Babu K, J.; Kulandaisamy, A.J.; Rayappan, J.B.B. Iron Oxide Nanoparticles: A Review on the Province of Its Compounds, Properties and Biological Applications. *Materials* **2023**, *16*, 59. [CrossRef]
62. Nurdini, N.; Ilmi, M.M.; Maryanti, E.; Setiawan, P.; Kadja, G.T.M.; Ismunandar. Thermally-induced color transformation of hematite: Insight into the prehistoric natural pigment preparation. *Heliyon* **2022**, *8*, e10377. [CrossRef]
63. Asghari, M.; Noaparast, M.; Chegeni, M.J. Implementation of DEM to calibrate contact parameters, as a novel simulation of the elastoplastic behavior of green iron pellet classified by roller screen. *Adv. Powder Technol.* **2024**, *35*, 104457. [CrossRef]
64. Reis, S.; Holliman, P.J.; Martin, C.; Jones, E. Biomass-Coal Hybrid Fuel: A Route to Net-Zero Iron Ore Sintering. *Sustainability* **2023**, *15*, 5495. [CrossRef]
65. Zhang, X.; Chen, Z.; Zhang, J.; Ding, P.; Zhou, J. Simulation and optimization of waste heat recovery in sinter cooling process. *Appl. Therm. Eng.* **2013**, *54*, 7–15. [CrossRef]
66. Tian, W.; Ni, B.; Jiang, C.; Wu, Z. Uncertainty analysis and optimization of sinter cooling process for waste heat recovery. *Appl. Therm. Eng.* **2019**, *150*, 111–120. [CrossRef]